Chemical Preintercalation of Magnesium Ions into α-MoO_3 Structure for Improved Electrochemical Stability in Li-Ion Cells

Darrell Omo-Lamai[1], Xinle Zhang[1], Ryan Andris[1], Michael J. Zachman[2], Ekaterina Pomerantseva[1*]

1. Department of Materials Science and Engineering, Drexel University, Philadelphia, PA 19104, USA
2. Center for Nanophase Materials Sciences, Oak Ridge National Laboratory, Oak Ridge, TN 37831, USA

* Corresponding Author: ep423@drexel.edu

Keywords:

MoO_3; Mg^{2+} preintercalation; interlayer engineering; electrochemical stabilization; lithium battery cathode

Abstract

Chemical preintercalation of layered materials, used as electrodes in intercalation-based energy storage devices, represents a promising strategy to enhance electrochemical stability and extend cycle life. However, standardized synthesis approaches for the chemical preintercalation of diverse ions into various layered materials are lacking, necessitating the development of specific synthesis routes for each ion and layered phase combination. In this study, we present the first successful demonstration of Mg^{2+} ion chemical preintercalation into the interlayer region of α-MoO_3, revealing its stabilizing effect during cycling in non-aqueous Li-ion cells. Using ethanol during hydrothermal treatment facilitated molybdenum reduction, which was critical for Mg^{2+} ion preintercalation. Interestingly, we found that Mg preintercalation was accompanied by the incorporation of water. Mg-preintercalated α-MoO_3 exhibited enhanced charge storage capacity, electrochemical stability, and power capability compared to pristine α-MoO_3 electrodes. This improved performance is attributed to the structural stabilization provided by Mg^{2+} pillars, which prevent undesirable phase transformations during repeated Li intercalation/deintercalation, and increased Li^+ ion diffusion due to the shielding of electrostatic interactions between electrochemically cycled ions and the α-MoO_3 lattice, enabled by structural water. Our study offers new insights into developing chemical preintercalation synthesis approaches that can be broadly applied to a wide range of pillaring ions and layered material hosts.

Graphical Abstract

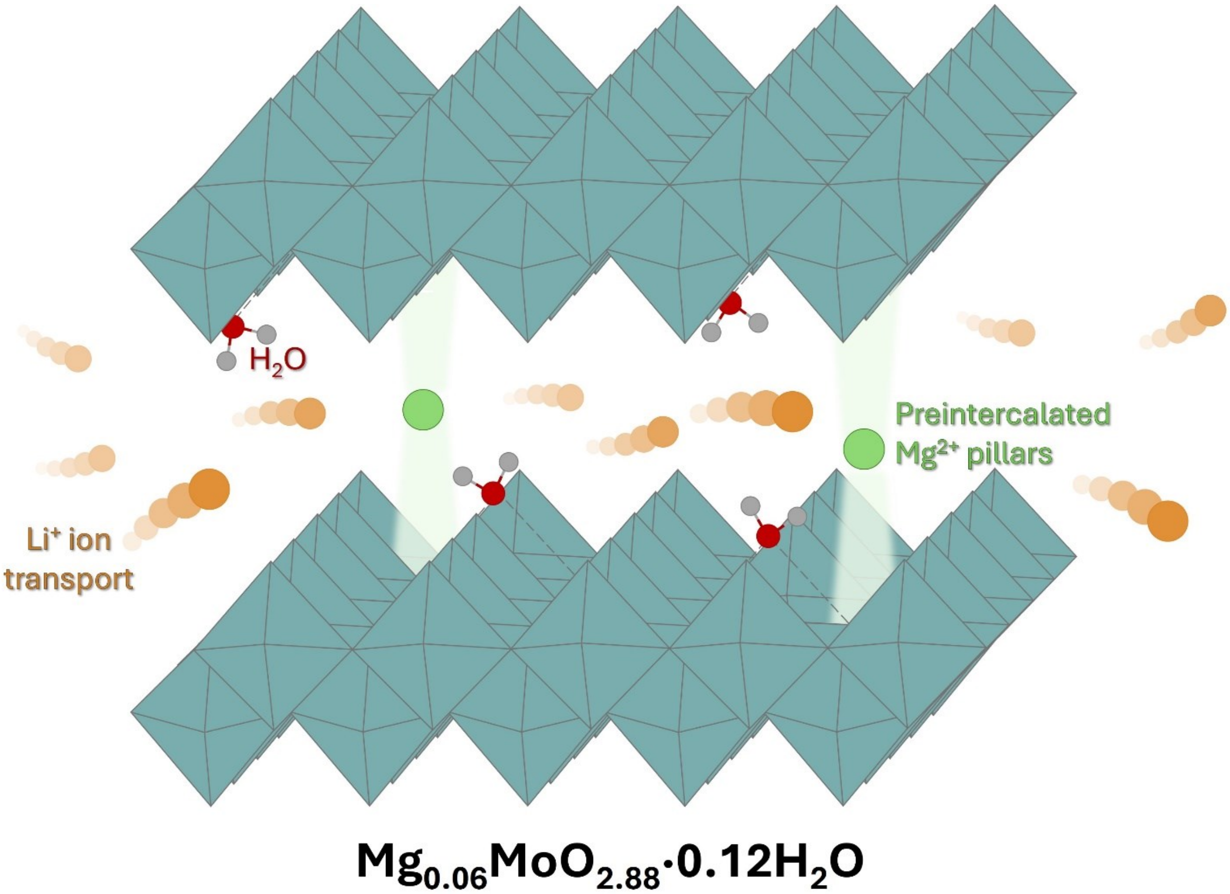

Introduction

The proliferation of portable electronic devices, the electrification of transportation, and the growing need for grid-scale renewable energy technologies have driven the demand for novel electrode materials that can repeatedly and reliably store energy as charges in electrochemical energy storage systems [1, 2]. Of the numerous electrode material chemistries that have been explored, layered transition metal oxides (LTMOs) that possess open channels for ion intercalation and are redox active with respectable theoretical specific capacities are established as the prominent candidates for electrochemical energy storage applications [3-5]. Nevertheless, despite their high theoretical capabilities, the performance of these materials is often hindered by practical challenges, with stability during electrochemical cycling being a significant concern [6, 7].

An efficient strategy for addressing the challenge of LTMO electrode instability in electrochemical systems is the chemical preintercalation of foreign species into the host oxide structure [8, 9]. The chemically preintercalated ions serve as pillars in the gallery space of the LTMO that enhance structural robustness during electrochemical intercalation and deintercalation [8, 10]. Previous reports have demonstrated the promise of this approach to stabilize LTMO systems. For instance, studies have demonstrated that advancements in the cycling stability of layered and tunneled manganese oxide (MnO_2) electrodes in Li-ion, K-ion, and Zn-ion cells can be realized through the synthetic preintercalation of K^+ ions, with the prepotassiated MnO_2 electrode materials showing suppressed phase transitions under electrochemical conditions and reduced dissolution in both aqueous and non-aqueous electrolytes [11-13]. Because of the ease of synthesis, chemical preintercalation is widely studied for bilayered vanadium oxide (BVO, δ-$V_2O_5 \cdot nH_2O$) electrodes; the electrochemical stabilization effect of chemically preintercalated alkali, alkaline-earth and transition metal ions has been demonstrated [14, 15]. The chemical preintercalation of Mg^{2+} ions into the BVO structure is of particular interest because it resulted in the greatest improvements in cycling stability [16, 17]. However, the bivalent nature of the magnesium ion presents inherent challenges that complicate its chemical preintercalation. Consequently, the process of incorporating Mg^{2+} ions into the interlayer region of other LTMOs presents considerable difficulties.

One extensively investigated LTMO electrode material with particularly promising properties is orthorhombic molybdenum trioxide (α-MoO_3). It crystallizes in the *Pbnm* space group, and its structure is characterized by bilayers of edge- and corner-sharing distorted MoO_6

octahedra separated by a van der Waals gap. Notably, its interlayer distance of 6.9 Å [18, 19] is larger than those of commonly employed active cathode materials such as lithium nickel manganese cobalt oxide and nickel cobalt aluminum oxide (4.7-4.8 Å) [20, 21], which is beneficial for ion diffusion. Furthermore, the high +6 oxidation state of Mo combined with a capability of multiple electron redox steps favors high-capacity charge storage [22]. However, the cycling performance of α-MoO_3 is limited by the aforementioned issue of electrochemical instability, with rapid capacity fading attributed to irreversible structural transformations and parasitic side reactions upon continuous cycling in both aqueous and non-aqueous electrochemical systems [23-25]. Stabilization strategies such as doping the electrode material at the transition metal site [26], creating heterointerfaces with conductive species [27, 28], incorporating anionic vacancies [29], and combining these approaches [30, 31] have been shown to substantially improve the electrochemical stability of transition metal-based electrode materials. However, these strategies cannot be easily applied to α-MoO_3 electrodes.

The chemical preintercalation approach has been shown to improve the stability of α-MoO_3. In the pioneering report of this strategy, it was found that α-MoO_3 preintercalated with Li^+ ions by stirring the pristine oxide in a LiCl solution followed by hydrothermal treatment at 180 °C showed 32 % greater capacity retention in a Li-ion cell after 15 cycles [19]. Similar improvements were observed in a study where Na^+ ions were preintercalated into α-MoO_3 by hydrothermally treating the oxide in a NaCl solution containing polyethylene glycol molecules at 180 °C and annealing the product at 400 ºC [18]. The amount of preintercalated Na^+ ions was tuned by varying the NaCl solution concentration, and interestingly, the greatest improvement in cycling stability in Li-ion cells (27.7 % greater capacity retention compared to pristine α-MoO_3 electrodes) was attained for the minute preintercalated Na^+ concentration of 0.072 Na atoms per Mo atom. Similarly prepared Na-preintercalated α-MoO_3 electrodes showed improved electrochemical stability in aqueous zinc/sodium batteries, with 79.2 % of specific capacity retaining after 500 cycles at 1 A g^{-1} as compared to 42.8 % for pristine α-MoO_3 cycled under the same conditions [32]. Additionally, successful chemical prepotassiation and its effect on charge storage properties was reported for the α-MoO_3 phase. Oxygen deficient K-preintercalated α-MoO_3 was synthesized by first hydrogenating α-MoO_3 in H_2/Ar at 350 °C followed by a reaction with KBH_4 in ethanol under stirring. The obtained K_yMoO_{3-x} allowed the intercalation of Li^+, Na^+, K^+ and Mg^{2+} ions from aqueous electrolytes [33]. In a separate study, different amounts of K^+ ions were chemically preintercalated into the α-MoO_3 structure by hydrothermally treating a mixture of $(NH_4)_6Mo_7O_{24}\cdot4H_2O$ with a certain amount of KCl in water/n-butyl alcohol at 180 °C, followed by annealing at 400°C in air to enhance the K_xMoO_3 crystallinity. To improve electronic conductivity, the obtained K-preintercalated molybdenum oxides were coated with carbon via sucrose treatment and subsequently annealed for carbonization. In the obtained K_xMoO_3@C series of materials, $K_{0.046}MoO_3$@C showed the highest electrochemical performance, with a capacity retention of 83.9 % after 500 cycles in Li-ion cells at a current density of 1500 mA g^{-1} [34]. Finally, another study discovered that composite electrodes composed of sulfur (S) and α-MoO_3 preintercalated with tin (Sn^{2+}) up to 0.063 Sn atoms per Mo atom by stirring the pristine oxide in a solution of $SnCl_2$, tartaric acid, and acetone showed extended cycle life capabilities in lithium-sulfur batteries compared to similar composite electrodes consisting of pristine α-MoO_3 and S [35]. The enhanced electrochemical performance of chemically preintercalated α-MoO_3 electrodes was attributed to improved structural stability enabled by the bonds between inserted metal ions and oxygen atoms in Mo-O layers, the enlarged size of the interlayer region, facilitating the diffusion of electrochemically cycled ions, and the mixed oxidation state of Mo, leading to increased electronic conductivity. However, there have been no reports of the chemical preintercalation of doubly charged alkaline earth metal ions – particularly, Mg^{2+} ions – into α-MoO_3. This leaves uncertainty regarding whether Mg^{2+} ions can be chemically inserted in the interlayer region of this phase and whether they can stabilize α-MoO_3 electrodes similarly to Li^+, Na^+ and K^+ ions.

Herein, we report synthesis conditions that allowed us to successfully incorporate Mg^{2+} ions into the structure of α-MoO_3 via a hydrogen peroxide-induced transformation of metallic molybdenum powder in the presence of $MgCl_2$ followed by hydrothermal treatment and annealing in air. Chemical preintercalation of magnesium was confirmed through comprehensive characterization of the material composition and structure. Mg_xMoO_3 electrodes showed improved specific capacities and cycling stability as compared to the pristine α-MoO_3 phase, affirming the ubiquitous stabilizing role of interlayer chemically preintercalated ions. The developed synthesis route offers promising prospects for realizing α-MoO_3 chemically preintercalated with various alkali and alkaline-earth ions. This approach holds potential for establishing relationships between the chemical composition, structure and charge storage properties of α-M_xMoO_3 (M = Li, Na, K, Mg, Ca) electrodes, not only in the Li-ion system but also across other types of intercalation batteries.

Experimental Methods

Synthesis of α-Mg_xMoO_3 and α-MoO_3 reference material

The developed synthesis approach is based on the method used to achieve chemical preintercalation of dopamine followed by carbonization to prepare α-$MoO_{3-\delta}$/C electrode materials [36]. To synthesize α-Mg_xMoO_3, 0.75 g of molybdenum (Mo) powder (Alfa Aesar) was dissolved in 7.5 ml of 4 M $MgCl_2$ (Fisher Scientific) aqueous solution via the dropwise addition of 7.5 ml of hydrogen peroxide solution (30 wt % H_2O_2, Alfa Aesar) over 1.5 h under continuous magnetic stirring. The $MgCl_2$ concentration was selected to ensure an excess of Mg^{2+} ions with respect to molybdenum concentration in the reacting mixture. Upon complete dissolution of Mo powder (~12 h), the resulting solution was transferred to a Teflon-lined autoclave to which 100 μL of ethanol was added. Ethanol concentration was limited to 100 μL to prevent molybdenum reduction to its +4 oxidation state and formation of MoO_2 phase. Hydrothermal treatment of this solution at 220 °C for 24 h produced a precipitate that was isolated by vacuum filtration with ~ 1000 ml of deionized water (15 MΩ) and dried at 105 °C for 5 h. The dry powder was ground with a mortar and pestle for 15 min. Finally, 150 mg of the powder material was placed in a box furnace and annealed in air at 400 °C for 5 h to fully oxidize reduced Mo species and enhance material crystallinity. The pristine α-MoO_3 material was synthesized similarly but in the absence of $MgCl_2$ in the initial dissolution step and ethanol in the hydrothermal treatment step.

Materials Characterization

Scanning electron microscopy (SEM) was used to image the particle morphology, and energy-dispersive X-ray spectroscopy (EDS) was used to analyze the materials' chemical composition. SEM images were collected using a Zeiss Supra 50VP (Germany) scanning electron microscope equipped with an EDS probe. EDS spectra were collected at a working distance of 15 mm and an accelerating voltage of 8 keV.

Atomic absorption spectroscopy (AAS) was used to quantitatively analyze the value of x in α-Mg_xMoO_3. The calibration curve was developed using 4 magnesium standard solutions with concentrations of 0.05, 0.10, 0.15, and 0.20 μg mL^{-1} prepared by diluting a 1000 μg mL^{-1}

magnesium standard with analytical grade water. The AAS sample was prepared by dissolving ~ 10 mg of ground α-Mg_xMoO_3 powder in a beaker with analytical grade deionized water by adding 1 drop of 30 wt % H_2O_2 (Alfa Aesar), sonicating for 10 min, then dispersing the solution in a 100 mL volumetric flask. The final concentration was determined by transferring 20 mL of the solution and further dispersing in a 100 mL volumetric flask. The magnesium concentration was analyzed using an AA-7000 flame atomic absorption spectrometer (Shimadzu, Japan) with acetylene as the fuel and compressed air as the supplementary gas. The magnesium cathode lamp was warmed up for 5 minutes in advance of the measurements.

X-ray diffraction (XRD) measurements were conducted using a Rigaku SmartLab X-ray diffractometer (Japan) with Cu Kα radiation to analyze the phase composition of the materials. The XRD patterns were collected in a 2θ range of 3° to 60° and with a step size of 0.02°. Powders of analyzed materials (pristine α-MoO_3 or α-Mg_xMoO_3) were mixed with a reference silicon (Si) powder in a 3:1 mass ratio for XRD measurements, and the Si diffraction peaks were used to align the diffractograms of the materials. Thermogravimetric analysis (TGA) measurements were performed in air from room temperature to 1000 ºC using a TA Instruments Q50 (TA Instruments, USA) instrument and a heating rate of 10 ºC min^{-1}. Fourier-transform infrared spectroscopy (FTIR) was used to gather further details on the structure and the chemical composition of the synthesized materials. Pellets for transmission FTIR measurements were prepared by grinding 0.5 mg of α-MoO_3 or α-Mg_xMoO_3 with 150 mg of KBr powder and pressing a 13 mm diameter pellet at 8 metric tons for 1 min. Transmittance spectra were obtained from 400 to 4,000 cm^{-1} using a Bruker Invenio® FTIR spectrometer. XPS measurements were recorded on a Physical Electronics VersaProbe 5000 using a monochromatic Al Kα source and Ar^+ charge compensation. The high-resolution spectra at Mo *3d*, O *1s*, and Mg *1s* regions were taken at a pass energy of 23.5 eV with a step size of 0.05 eV. Peak fitting and data analysis were carried out using CasaXPS software. A linear background was applied for quantification analysis. Scanning transmission electron microscopy (STEM) images and energy-dispersive X-ray spectroscopy (EDS) maps were acquired on a JEOL NEOARM aberration-corrected analytical STEM in the Center for Nanophase Materials Sciences (CNMS) at Oak Ridge National Laboratory (ORNL) that is equipped with dual JEOL SDD EDS detectors. The instrument was operated at 200 keV with a semiconvergence angle of ~ 28 mrad and EDS. JEOL Analysis Station was used to generate elemental maps by binning the data in real space from 512 × 512 to 64 × 64 to increase the signal-to-noise ratio and displaying the background-subtracted net intensities of the relevant elements.

Electrochemical Testing and Analysis

Electrochemical testing was performed using the 2032-type coin cell configuration. The working electrodes were fabricated by casting slurries which contained 80 wt % of active material, 10 wt % of carbon black, and 10 wt % of poly(vinylidene fluoride) (PVDF, Kynar Flex, Arkema, USA) on aluminum foil. The working electrodes were dried at 105 °C under vacuum overnight, and then transferred to an argon-filled glove box. The current densities and specific capacities exhibited by the cells were normalized by 80 wt % of the dried electrode mass in agreement with the active material content. Lithium metal chips (99.9 %, battery grade, AOT Battery Technology) were used as both counter and reference electrodes. Potentials are reported with respect to the Li/Li^+ reference couple. LP40 (Gotion, USA) and Celgard 2325 served as the electrolyte and the separator, respectively. Cyclic voltammetry (CV) curves were acquired using a Biologic VMP3 potentiostat, and galvanostatic cycling tests were performed using a multichannel electrochemical workstation (Arbin Instruments, USA) within a voltage window of 1.5 to 3.5 V. All cells were rested for 1 h upon assembly and cycled at room temperature. The electrochemical impedance spectroscopy (EIS) experiments were performed using VMP3 potentiostat (Biologic, USA) by applying a sinusoidal alternating potential in a frequency range between 10 mHz and 200 kHz. The data were acquired during the first (at open circuit voltage (OCV), 0% state-of-charge (SOC), and 100% SOC) and tenth (at 0% SOC and 100% SOC) galvanostatic discharge/charge cycles in a potential window of 1.5 – 3.5 V vs Li/Li^+ at a current density of $100\ mA\cdot g^{-1}$.

Results and Discussion

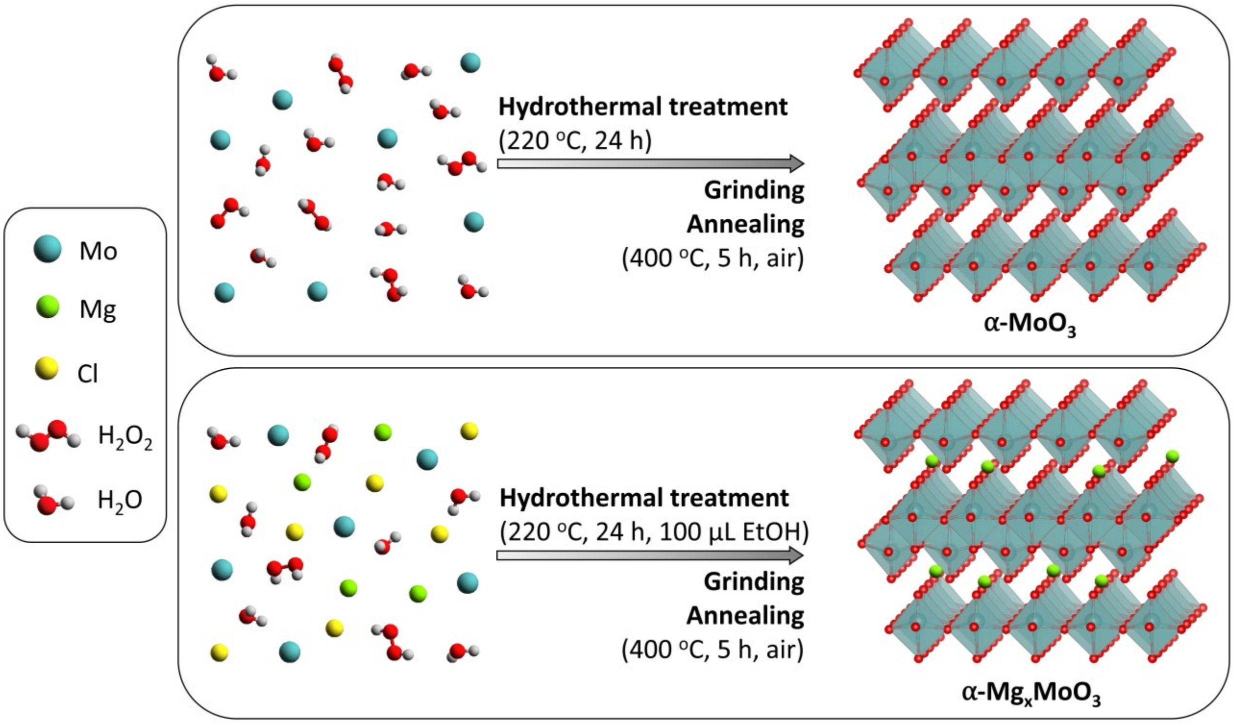

Figure 1. Schematic illustration of the approach to synthesizing pristine α-MoO_3 (top panel) and Mg-preintercalated α-MoO_3 (α-Mg_xMoO_3, bottom panel).

Chemical preintercalation of Mg^{2+} ions into α-MoO_3 structure was enabled by modifying synthesis parameters starting from the conditions used to prepare pristine α-MoO_3 nanobelts and α-$MoO_{3-\delta}$/C nanoflowers [36, 37]. Specifically, ethanol was added to the synthesis mixture during the hydrothermal treatment step to facilitate molybdenum reduction, which is needed to incorporate additional positive charge brought by Mg^{2+} ions. A similar strategy was used to achieve chemical prepotassiation of α-MoO_3 [33]. Additionally, the material obtained after hydrothermal treatment was thoroughly ground and annealed at 400 ºC in air to enhance the crystallinity of the samples, similar to the K-preintercalated α-MoO_3 [34]. The strategies adopted to synthesize the pristine α-MoO_3 material and the Mg-containing α-Mg_xMoO_3 material are shown schematically in **Figure 1**, while characteristic digital photographs of the specimens before and after Mo dissolution, after hydrothermal treatment at 220 ºC, and after annealing in air at 400 ºC are depicted in **Figure S1 (Supporting Information)**. In the case of α-MoO_3, the dissolution of Mo resulted in a transparent yellow solution. Hydrothermal treatment at 220 ºC for 24 h produced an off-white powder and annealing at 400 ºC for 5 h in air produced a white α-MoO_3 material. In the case of α-Mg_xMoO_3, the differences in reaction pathways and final product, as compared to α-MoO_3, were obvious from visual observations (**Figure S1, Supporting Information)**. The initial dark grey suspension consisting of Mo particles dispersed in a 4 M $MgCl_2$ solution transformed to a clear, brick-orange solution upon complete Mo dissolution. Hydrothermal treatment of this solution at 220 ºC for 24 h with the addition of 100 μL ethanol resulted in a dark blue powder while annealing at 400 ºC for 5 h in air produced a light blue/grey α-Mg_xMoO_3 material.

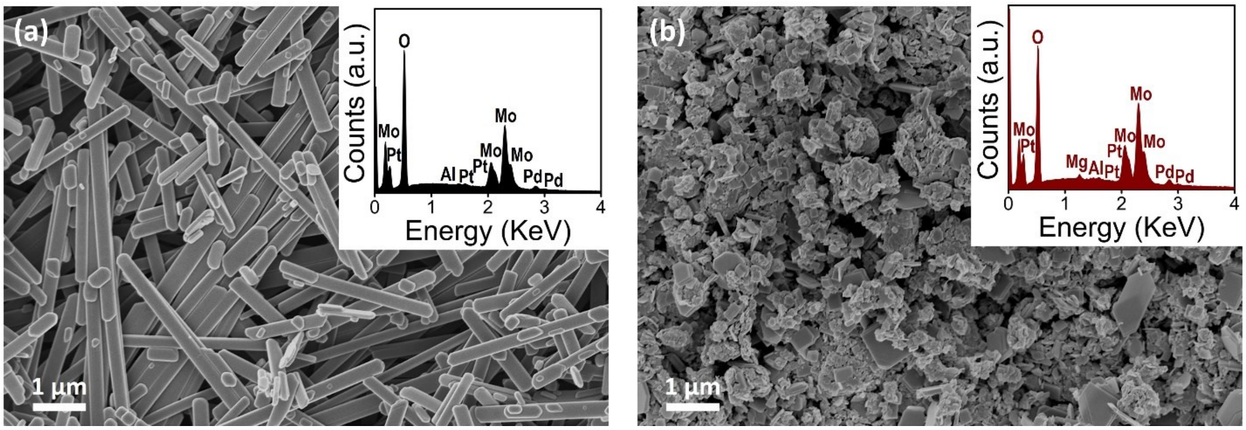

Figure 2. SEM images of (a) pristine α-MoO_3 and (b) α-Mg_xMoO_3 particles. Corresponding EDS maps are shown as insets.

SEM images of pristine α-MoO_3 and α-Mg_xMoO_3 powders are shown in **Figure 2**, with characteristic EDS maps presented as insets. α-MoO_3 (**Figure 2a**) crystallizes as nanobelts, with the lengths of the nanobelts varying from 100 nm to over 5 μm because of the grinding process adopted prior to the final annealing step during synthesis. This morphology has been widely reported for α-MoO_3 synthesized through aqueous dissolution and hydrothermal reactions [36-39]. The corresponding EDS map (**Figure 2a, inset**) shows prominent peaks at 0.5 KeV and 2.3 KeV that confirm the presence of O and Mo atoms, respectively. Unlike α-MoO_3, which adopts a uniform particle morphology, α-Mg_xMoO_3 displays two distinct morphologies consisting of spherical agglomerates of nanometer-sized particles interspaced with larger intimately interfacing micron-sized platelets, with the former being more abundant (**Figure 2b**). The platelets resemble segments of nanobelts, similar to those observed in the SEM images of α-MoO_3, presumably formed through the grinding of original, long nanobelts. In addition to the aforementioned Mo and O signals, a peak at 1.3 KeV that is indicative of Mg presence is observed in the corresponding EDS map of α-Mg_xMoO_3. An analysis of the relative Mg and Mo atomic percentages determined using AAS measurements revealed a Mg/Mo atomic ratio of 0.0598 (**Figure S2, Table S1**). This order of magnitude of preintercalated ions is consistent with those reported in previous studies of α-MoO_3 with Na^+, K^+ and Sn^+ ions, with 0.072 Na, 0.046 K and 0.028 Sn atoms preintercalated per Mo atom, respectively [18, 34, 35]. For further discussion, we will round this value to 0.06 and represent the Mg preintercalation degree with the chemical formula of α-$Mg_{0.06}MoO_3$. The phenomenon of dual morphology evinced by α-$Mg_{0.06}MoO_3$ is explainable by the hypothesis that the agglomerated particles are Mg-preintercalated α-MoO_3, while the particles with the platelet morphology, that is reminiscent of pristine α-MoO_3 particles, correspond to those where Mg-preintercalation did not occur. Indeed, this suggests the coexistence of Mg-containing structures and non-Mg-containing structures in α-$Mg_{0.06}MoO_3$.

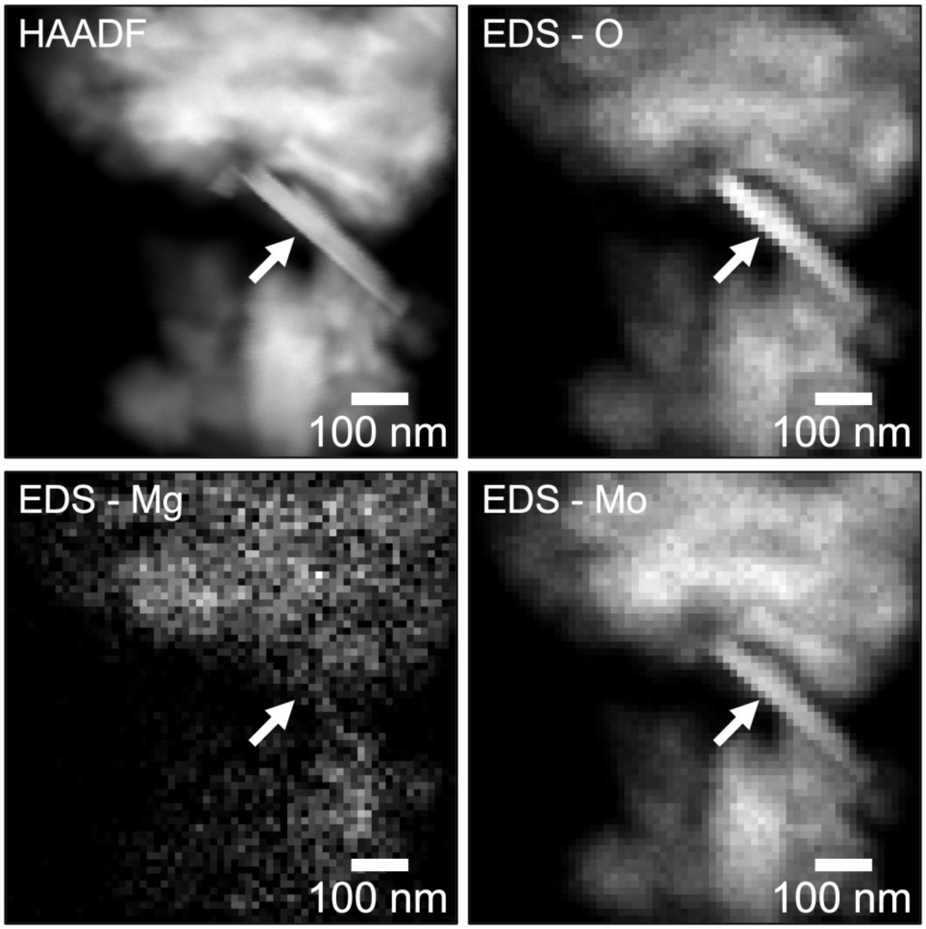

Figure 3. HAADF-STEM image and corresponding EDS elemental maps of O, Mg, and Mo in the α-$Mg_{0.06}MoO_3$ material. Arrows indicate a nanobelt, which contained significantly less Mg than the surrounding spherical agglomerate regions.

The proposed correlation between the particle morphologies and chemical composition was verified via STEM imaging combined with EDS mapping. **Figure 3** shows a high-angle annular dark-field (HAADF) STEM image of a region containing both a nanobelt and spherical agglomerates in α-$Mg_{0.06}MoO_3$ (a second region is displayed in **Figure S3**). STEM-EDS revealed that the spherical agglomerate particles had a significantly higher Mg content than the nanobelts. These observations were consistent across the material – with a combination of nanobelts and spherical agglomerates present, spherical agglomerates were generally more prevalent than nanobelts, and spherical agglomerates had higher Mg content. Despite the presence of a small fraction of non-premagnesiated phase in the material synthesized with $MgCl_2$, we will call it α-$Mg_{0.06}MoO_3$ throughout the manuscript to distinguish it from the reference α-MoO_3 material.

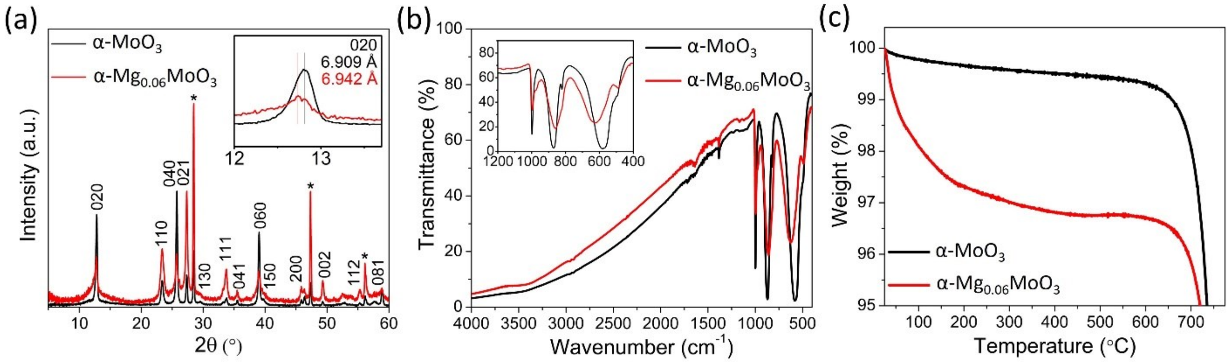

Figure 4. Structural and chemical analysis of pristine α-MoO_3 and α-$Mg_{0.06}MoO_3$ materials. (a) XRD patterns with reflections indexed to the orthorhombic MoO_3 phase (α-MoO_3, JCPDS No. 05-0508) in the *Pbnm* space group and the *(020)* reflection of both materials shown in the inset. The asterisked reflections are from a reference Si powder. (b) FTIR spectra from 400 to 4000 cm^{-1}, with the spectra from 400 to 1200 cm^{-1} shown in the inset. (c) TGA weight loss curves; the temperature range is chosen to avoid showing a 100% weight drop caused by α-MoO_3 sublimation above 700 °C.

X-ray diffractograms for the pristine α-MoO_3 and α-$Mg_{0.06}MoO_3$ are shown in **Figure 4a**. The diffractograms of both materials show similar patterns, with prominent peaks that are indexed to the orthorhombic MoO_3 (α-MoO_3, JCPDS No. 05-0508) phase. Nevertheless, peaks in the XRD pattern of α-$Mg_{0.06}MoO_3$ generally have wider full widths at half maximum, indicating greater disorder in its crystal structure likely due to the effect of sparsely preintercalated Mg^{2+} ions on the periodicity of the crystal structure. The difference in peak intensities observed in the XRD patterns of α-MoO_3 and α-$Mg_{0.06}MoO_3$ phases are caused by the texturing effect typical for α-MoO_3

nanobelts, which is not as pronounced in the case of the α-$Mg_{0.06}MoO_3$ powder. In the latter, the predominantly spherical agglomerates do not show a tendency to adopt a specific orientation (**Figure 2b**). The absence of discernable secondary phases in the diffractogram of α-$Mg_{0.06}MoO_3$ supports the proposition that both morphologies exhibited by the material are of an α-MoO_3 crystal structure, with the morphological differences occurring due to Mg-preintercalation in the regions where particle agglomeration is observed. Interestingly, as shown by the inset in the XRD graph, an increase of only ~ 0.034 Å is observed in the *(020)* d-spacing of α-$Mg_{0.06}MoO_3$ compared to pristine α-MoO_3. In the seminal study of Li-preintercalated α-MoO_3, lithiation resulted in a similar (*020)* d-spacing increase of 0.065 Å [19]. The finding in the present study thereby suggests that the comparatively smaller ionic radius and higher charge density of Mg^{2+} results in increased electrostatic attractions between the preintercalated species and the host bilayers upon the introduction of Mg^{2+} into the interlayer region.

Figure 4b presents the FTIR spectra of pristine α-MoO_3 and α-$Mg_{0.06}MoO_3$. The spectra of both materials are consistent with those reported in existing studies of the structure of α-MoO_3. The band near 1000 cm^{-1} arises due to the vibrations of Mo=terminal O bonds. The bands near 870 and 600 cm^{-1} are attributable to the vibrational modes of bridging Mo-O bonds in which O atoms are linked to two and three Mo atoms, respectively [19, 40]. The α-$Mg_{0.06}MoO_3$ FTIR spectrum shows no additional vibrational modes and no discernable vibrations from a secondary crystal structure, thereby further confirming that the chemical preintercalation of small amounts of Mg into α-MoO_3 as performed in this study produces minimal changes to the host crystal structure. Nevertheless, small shifts in peak widths and peak positions, such as those observed for the peak corresponding to Mo-O bond vibrations where O atoms are linked to three Mo atoms and for which the peak is centered at 584 cm^{-1} in the pristine α-MoO_3 material but at 623 cm^{-1} in the α-$Mg_{0.06}MoO_3$ material, indicate slight variations in the local environments of the materials, likely arising due to the presence of Mg^{2+} ions.

TGA weight loss curves for pristine α-MoO_3 and α-$Mg_{0.06}MoO_3$ powders are shown in **Figure 4c**. A notable distinction is evident in the weight loss patterns of the materials up to 475 ºC, with greater loss occurring for α-$Mg_{0.06}MoO_3$ compared to α-MoO_3. The weight loss below 100 °C is attributed to physically adsorbed surface water, and the difference in weight loss behavior in this temperature region is likely caused by the different morphologies of α-MoO_3 and α-$Mg_{0.06}MoO_3$ powders (**Figure 2**). However, α-$Mg_{0.06}MoO_3$ continues losing ~ 1.45% of its weight between 100 °C and 475 °C (**Figure S4**, **Supporting Information**), after which the weight stabilizes up to ~ 700°C. The complete weight loss above this temperature is caused by α-MoO_3 sublimation [41, 42]. A previous study found that chemical preintercalation of inorganic ions into bilayered vanadium oxide was accompanied by the incorporation of water molecules into the interlayer region, and evaporation of such interlayer water was associated with the weight loss in a similar temperature region [17]. Moreover, water incorporation into the interlayer region of the α-MoO_3 structure was achieved via a complex process involving reduction of α-MoO_3 using *n*-butyllithium followed by oxidation using water [43]. Interestingly, in the case of α-MoO_3 hydration, it was found that H_2O molecules take the place of lattice oxygen. Therefore, the composition of the sample was best represented by chemical formulas from $MoO_{2.81}\cdot0.19H_2O$ to $MoO_{2.63}\cdot0.37H_2O$, depending on the degree of hydration. We believe that a similar mechanism of water incorporation accompanies Mg preintercalation in our synthesis route, resulting in a material with a chemical composition best described by the formula of α-$Mg_{0.06}MoO_{2.88}\cdot0.12H_2O$, which is in good agreement with the 1.45% weight loss due to the evaporation of water between 100 °C and 475 °C (**Figure S4**, **Supporting Information**). The presence of water molecules in the interlayer region of Mg-preintercalated α-MoO_3 is also confirmed by FTIR data (**Figure 4b**). The low-intensity peaks at ~1600 cm^{-1} and ~3400 cm^{-1} that appear in the FTIR spectrum of α-$Mg_{0.06}MoO_3$ and are not visible in the FTIR spectrum of α-MoO_3 correspond to the bending H-O-H and stretching H-O vibrations of the interlayer water molecules, respectively. For consistency, we will continue using the α-$Mg_{0.06}MoO_3$ notation to indicate the Mg-preintercalated α-MoO_3 synthesized in this work throughout the manuscript.

Figure 5 shows the results of XPS characterization of α-$Mg_{0.06}MoO_3$, with the survey XPS spectrum confirming the presence of Mo, O and Mg peaks shown in **Figure 5a**. The high-resolution XPS spectrum of Mo 3d (**Figure 5b**) revealed that the peaks at the binding energies of 232.59 eV and 235.73 eV were the characteristic Mo $3d_{5/2}$ and Mo $3d_{3/2}$ of Mo^{6+}, respectively. No molybdenum reduction was suggested by XPS analysis. We believe that while Mg preintercalation reduces Mo, forming oxygen vacancies, the co-intercalated water molecules oxidize Mo. As a result, no net oxidation state change occurs, and Mo is present in the structure of α-$Mg_{0.06}MoO_3$ (correctly represented as α-$Mg_{0.06}MoO_{2.88}\cdot0.12H_2O$) in the oxidation state of 6+ as observed in the XPS spectra. **Figure 5c** shows that the O 1s XPS signal is split into two peaks at 530.42 eV and 531.62 eV that correspond to oxygen bound to Mo from Mo-O layers and oxygen from the interlayer water bound to Mo, in agreement with previous studies of hydrated α-MoO_3 [43, 44]. The high-resolution XPS spectrum of Mg 1s (**Figure 5d**) at 1304.04 eV further confirms the presence of Mg in the α-$Mg_{0.06}MoO_3$ structure achieved via the developed synthesis approach.

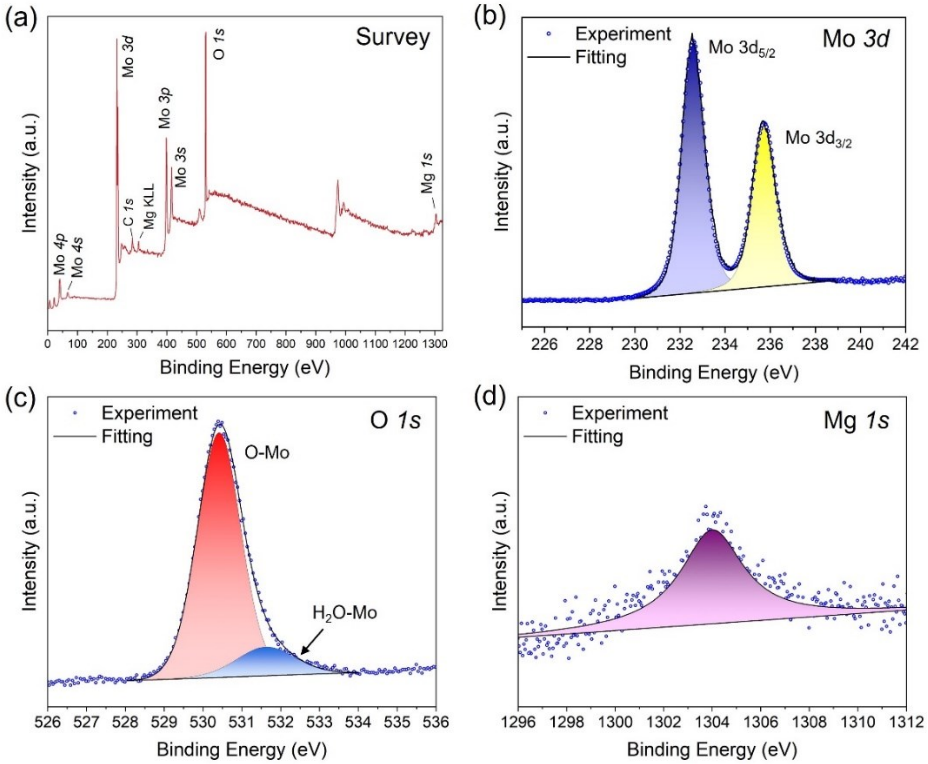

Figure 5. XPS analysis of the (a) survey spectrum and fitted spectra in (b) Mo 3d, (c) O 1s, and (d) Mg 1s regions of the α-$Mg_{0.06}MoO_3$ phase.

To investigate the effects of Mg preintercalation on the electrochemical properties of α-MoO_3, cyclic voltammetry experiments at a scan rate of 0.1 mV s^{-1} over the potential range of 1.5 – 3.5 V were performed. The first- and second-cycle CV curves of the pristine α-MoO_3 and α-$Mg_{0.06}MoO_3$ electrodes are shown in **Figure 6a** and **6b**, respectively. In general, the preintercalation of Mg^{2+} does not significantly affect the lithium-ion intercalation potentials, as the two electrodes exhibit a similar CV curve that is consistent with previous reports [25, 34, 42, 45-49]. The first discharge cycle of both electrode materials exhibits a two-step lithiation process, with two cathodic peaks appearing at ~2.68 V and ~2.20 V (**Figure 6a**). However, both electrode materials only exhibit one peak at 2.50 – 2.60 V on first charge, and only one redox pair at 2.05 V on discharge and 2.48 – 2.55 V on charge is observed in the subsequent cycles (**Figure 6b**).

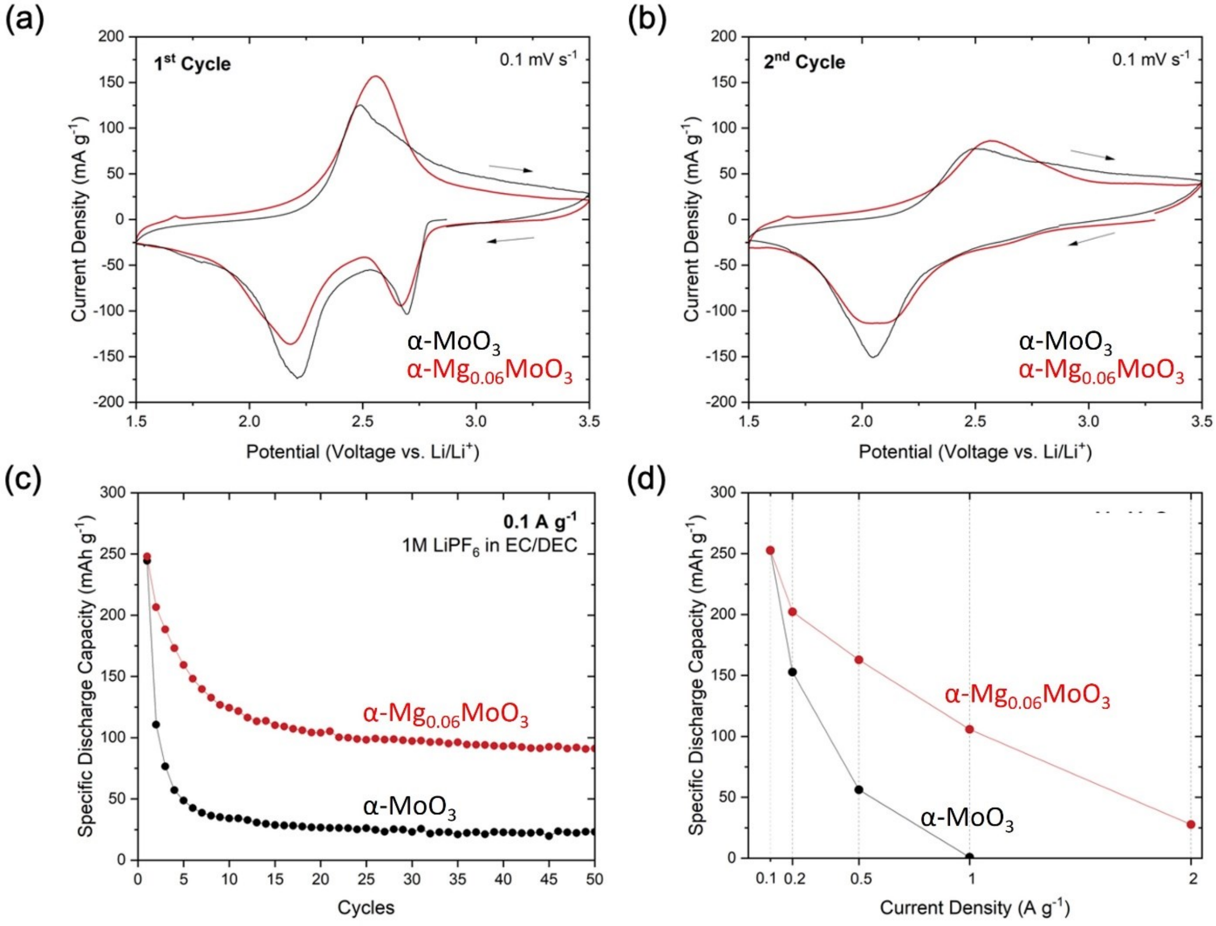

Figure 6. Electrochemical performance of α-MoO_3 and α-$Mg_{0.06}MoO_3$ electrodes in Li-ion cells showing (a) 1st cycle and (b) 2nd cycle cyclic voltammetry curves of the electrode materials at 0.1 mV s^{-1}; (c) cycle life specific discharge capacities at 0.1 A g^{-1}; and (d) rate capability specific discharge capacities at increasing current densities of 0.1, 0.2, 0.5, 1, and 2 A g^{-1}.

The disappearance of the cathodic peak around ~2.68 V after first discharge is a well-documented phenomenon for α-MoO_3 electrodes in Li-ion cells. It is attributed to the irreversible insertion of Li^+ ions into the intralayer sites of α-MoO_3 structure, causing structural transformation and altered electrochemical behavior on the second and subsequent cycles [18, 34, 42, 46-49]. As a result, the cell containing the α-MoO_3 electrode shows a large first-to-second cycle capacity drop, while the cell with the α-$Mg_{0.06}MoO_3$ electrode exhibits improved first-to-second cycle stability, as confirmed through galvanostatic cycling at a current density of 0.1 A g^{-1} (**Figure 6c**). Both phases delivered a comparable discharge capacity of ~250 mAh g^{-1} on the first cycle. However, the α-MoO_3 electrode showed a second cycle discharge capacity of only 112 mAh g^{-1}, which is significantly lower than the 207 mAh g^{-1} exhibited by the α-$Mg_{0,06}MoO_3$ electrode on the second discharge cycle. Moreover, the cell containing α-$Mg_{0.06}MoO_3$ demonstrated improved capacity retention after 50 discharge/charge cycles, with the α-$Mg_{0.06}MoO_3$ electrode delivering ~ 100 mAh g^{-1} and the α-MoO_3 electrode retaining only ~20 mAh g^{-1} (**Figure 6c**). The improved electrochemical stability of the α-$Mg_{0.06}MoO_3$ electrode is attributed to the stabilizing effect of chemically preintercalated Mg^{2+} ions on the charge storage behavior of α-MoO_3. We believe that similarly to chemically preintercalated Li^+, Na^+ and K^+ ions [18, 19, 32-34], Mg^{2+} ions serve as electrochemically inactive pillars upon cycling α-MoO_3 in Li-ion cells, thereby enabling improved structural stability upon extended electrochemical cycling [8]. Additionally, it is probable that the dissolution of the active material in the non-aqueous electrolyte – a significant cause of capacity fading in α-MoO_3 [7] – is suppressed due to the preintercalation of Mg^{2+} ions. To evaluate the ability of α-$Mg_{0.06}MoO_3$ to operate at high currents and understand the effect of chemically preintercalated Mg^{2+} ions, both α-$Mg_{0.06}MoO_3$ and α-MoO_3 electrodes were cycled at the increasing current densities of 0.1, 0.2, 0.5, 1.0, and 2.0 A g^{-1} (**Figure 6d**). α-MoO_3 electrodes stored no charge beyond 1 A g^{-1}. However, the cells containing α-Mg_xMoO_3 electrodes not only retained a capacity of over 100 mAh g^{-1} at 1 A g^{-1}, but also delivered a capacity of ~28 mAh g^{-1} at 2 A g^{-1}. This finding could indicate that chemically preintercalating Mg^{2+} into α-MoO_3 promotes charge migration through the material during electrochemical cycling even under diffusion-limiting high current conditions. Additionally, incorporated water molecules that accompanied chemically preintercalated Mg^{2+} ions have the ability to shield electrostatic interactions between electrochemically cycled Li^+ ions and the Mo-O layered network [43, 44]. Electrochemical impedance spectroscopy measurements further attest that chemically preintercalated Mg^{2+} ions and water molecules enhance the conductivity and electrochemical kinetics of α-MoO_3 electrodes (**Figure S5**, **Supporting Information**). Therefore, the superior electrochemical behavior of the α-$Mg_{0.06}MoO_3$ electrodes could be attributed to interlayer water and the structure stabilization effect of Mg^{2+} ions.

Conclusions

Mg-preintercalated α-MoO_3 has been successfully prepared through H_2O_2-assisted dissolution of metallic molybdenum powder in the presence of $MgCl_2$ followed by hydrothermal treatment with the addition of a minute amount of ethanol, grinding, and annealing at 400 °C in air. Analyses of XRD patterns, TGA weight loss curves, AAS, EDX, FTIR and XPS spectra revealed that Mg^{2+} ions are co-intercalated into the interlayer region of α-MoO_3 structure together with water molecules, producing a material with a chemical formula of α-$Mg_{0.06}MoO_{2.88}\cdot 0.12H_2O$. SEM imaging demonstrated that the obtained material has a dual morphology dominated by spherical agglomerates of nanometer-sized particles with a small fraction of micron-sized platelets. From analyses of STEM images combined with EDX mapping, it was found that the spherical agglomerates correspond to the Mg-preintercalated α-MoO_3, while the platelets represent the pristine α-MoO_3 phase. Chemical co-preintercalation of Mg^{2+} ions and H_2O molecules was shown to be an efficient strategy to improve the electrochemical stability of α-MoO_3 electrodes in non-aqueous Li-ion cells. A 32 % improvement in specific capacity after 50 cycles at a current density of 0.1 A g^{-1} and a 43 % improvement in specific capacity at a current density of 1 A g^{-1} was achieved by premagnesiation of α-MoO_3. The improved electrochemical performance is attributed to the stabilization of the α-MoO_3 structure by the incorporation of Mg^{2+} and H_2O pillars and the shielding effect of interlayer H_2O molecules leading to facilitated diffusion of Li^+ ions. We believe that the developed synthesis approach can be adapted to synthesize α-MoO_3 chemically preintercalated with various types of ions and used to explore correlations between the nature of chemically preintercalated ions and charge storage properties. The obtained chemically preintercalated α-MoO_3 electrodes have the potential to show advanced performance in other energy storage systems, such as aqueous Zn-ion batteries, and for applications in electrochromics, photocatalysis, and gas sensing.

Acknowledgments

This work was supported by the National Science Foundation grant DMR-2106445. XRD, SEM and XPS analyses were performed using instruments in the Materials Characterization Core at Drexel University. The scanning transmission electron microscopy/energy-dispersive X-ray spectroscopy portion of this research was supported by the Center for Nanophase Materials Sciences (CNMS), which is a US Department of Energy, Office of Science User Facility at Oak Ridge National Laboratory.

References

1. Liu, C., F. Li, L.P. Ma, and H.M. Cheng, *Advanced materials for energy storage.* Advanced materials, 2010. **22**(8): p. E28-E62.

2. Pomerantseva, E., F. Bonaccorso, X. Feng, Y. Cui, and Y. Gogotsi, *Energy storage: The future enabled by nanomaterials.* Science, 2019. **366**(6468): p. eaan8285.

3. Nanda, J. and V. Augustyn, *Transition metal oxides for electrochemical energy storage*. 2022: John Wiley & Sons.

4. Yuan, S., X. Duan, J. Liu, Y. Ye, F. Lv, T. Liu, Q. Wang, and X. Zhang, *Recent progress on transition metal oxides as advanced materials for energy conversion and storage.* Energy Storage Materials, 2021. **42**: p. 317-369.

5. Zhang, M., D.A. Kitchaev, Z. Lebens-Higgins, J. Vinckeviciute, M. Zuba, P.J. Reeves, C.P. Grey, M.S. Whittingham, L.F. Piper, and A. Van der Ven, *Pushing the limit of 3d transition metal-based layered oxides that use both cation and anion redox for energy storage.* Nature Reviews Materials, 2022. **7**(7): p. 522-540.

6. Kim, J.-M., X. Zhang, J.-G. Zhang, A. Manthiram, Y.S. Meng, and W. Xu, *A review on the stability and surface modification of layered transition-metal oxide cathodes.* Materials Today, 2021. **46**: p. 155-182.

7. Cao, Y., Y. He, H. Gang, B. Wu, L. Yan, D. Wei, and H. Wang, *Stability study of transition metal oxide electrode materials.* Journal of Power Sources, 2023. **560**: p. 232710.

8. Pomerantseva, E., *Chemical preintercalation synthesis of versatile electrode materials for electrochemical energy storage.* Accounts of Chemical Research, 2022. **56**(1): p. 13-24.

9. Yao, X., Y. Zhao, F.A. Castro, and L. Mai, *Rational Design of Preintercalated Electrodes for Rechargeable Batteries.* ACS Energy Letters, 2019. **4**(3): p. 771-778.

10. Liu, Y., J. Xu, J. Li, Z. Yang, C. Huang, H. Yu, L. Zhang, and J. Shu, *Pre-intercalation chemistry of electrode materials in aqueous energy storage systems.* Coordination Chemistry Reviews, 2022. **460**: p. 214477.

11. Zhao, Q., A. Song, S. Ding, R. Qin, Y. Cui, S. Li, and F. Pan, *Preintercalation strategy in manganese oxides for electrochemical energy storage: review and prospects.* Advanced Materials, 2020. **32**(50): p. 2002450.

12. Lin, B., X. Zhu, L. Fang, X. Liu, S. Li, T. Zhai, L. Xue, Q. Guo, J. Xu, and H. Xia, *Birnessite nanosheet arrays with high K content as a high-capacity and ultrastable cathode for K-ion batteries.* Advanced Materials, 2019. **31**(24): p. 1900060.

13. Liu, G., H. Huang, R. Bi, X. Xiao, T. Ma, and L. Zhang, *K^+ pre-intercalated manganese dioxide with enhanced Zn^{2+} diffusion for high rate and durable aqueous zinc-ion batteries.* Journal of Materials Chemistry A, 2019. **7**(36): p. 20806-20812.

14. Sun, Q., H. Cheng, W. Nie, X. Lu, and H. Zhao, *A Comprehensive Understanding of Interlayer Engineering in Layered Manganese and Vanadium Cathodes for Aqueous Zn-Ion Batteries.* Chemistry – An Asian Journal, 2022. **17**(7): p. e202200067.

15. Jiang, W., K. Zhu, and W. Yang, *Critical Issues of Vanadium-Based Cathodes Towards Practical Aqueous Zn-Ion Batteries.* Chemistry – A European Journal, 2023. **29**(56): p. e202301769.

16. Clites, M. and E. Pomerantseva, *Bilayered vanadium oxides by chemical pre-intercalation of alkali and alkali-earth ions as battery electrodes.* Energy Storage Materials, 2018. **11**: p. 30-37.

17. Ridley, P., C. Gallano, R. Andris, C.E. Shuck, Y. Gogotsi, and E. Pomerantseva, *MXene-derived bilayered vanadium oxides with enhanced stability in Li-ion batteries.* ACS Applied Energy Materials, 2020. **3**(11): p. 10892-10901.

18. Dong, Y., X. Xu, S. Li, C. Han, K. Zhao, L. Zhang, C. Niu, Z. Huang, and L. Mai, *Inhibiting effect of Na^+ pre-intercalation in MoO_3 nanobelts with enhanced electrochemical performance.* Nano Energy, 2015. **15**: p. 145-152.

19. Mai, L.Q., B. Hu, W. Chen, Y. Qi, C. Lao, R. Yang, Y. Dai, and Z.L. Wang, *Lithiated MoO_3 nanobelts with greatly improved performance for lithium batteries.* Advanced Materials, 2007. **19**(21): p. 3712-3716.

20. Liu, W., M. Qin, C. Gao, D. Yu, and Y. Yue, *Green and low-cost synthesis of $LiNi_{0.8}Co_{0.15}Al_{0.05}O_2$ cathode material for Li-ion batteries.* Materials Letters, 2019. **246**: p. 153-156.

21. Sun, H. and K. Zhao, *Electronic Structure and Comparative Properties of $LiNi_xMn_yCo_zO_2$ Cathode Materials.* The Journal of Physical Chemistry C, 2017. **121**(11): p. 6002-6010.

22. Tsumura, T. and M. Inagaki, *Lithium insertion/extraction reaction on crystalline MoO_3.* Solid State Ionics, 1997. **104**(3-4): p. 183-189.

23. Wang, L., S. Yan, C.D. Quilty, J. Kuang, M.R. Dunkin, S.N. Ehrlich, L. Ma, K.J. Takeuchi, E.S. Takeuchi, and A.C. Marschilok, *Achieving stable molybdenum oxide cathodes for aqueous zinc-ion batteries in water-in-salt electrolyte.* Advanced Materials Interfaces, 2021. **8**(9): p. 2002080.

24. Zhang, G., T. Xiong, M. Yan, L. He, X. Liao, C. He, C. Yin, H. Zhang, and L. Mai, *α-MoO_{3-x} by plasma etching with improved capacity and stabilized structure for lithium storage.* Nano Energy, 2018. **49**: p. 555-563.

25. Chen, J.S., Y.L. Cheah, S. Madhavi, and X.W. Lou, *Fast synthesis of α-MoO_3 nanorods with controlled aspect ratios and their enhanced lithium storage capabilities.* The Journal of Physical Chemistry C, 2010. **114**(18): p. 8675-8678.

26. Huang, G.-X., R.-H. Wang, X.-Y. Lv, J. Su, Y.-F. Long, Z.-Z. Qin, and Y.-X. Wen, *Effect of niobium doping on structural stability and electrochemical properties of $LiNiO_2$ cathode for Li-ion batteries.* Journal of The Electrochemical Society, 2022. **169**(4): p. 040533.

27. Zhang, Y.-N., Y. Zhou, J. Su, Y.-F. Long, X.-Y. Lv, H.-X. Kuai, and Y.-X. Wen, *Co-Fe hydroxyoxalate nanosheets chemically bonded with reduced graphene oxide as high-performance anode for lithium-ion batteries.* Applied Surface Science, 2022. **585**: p. 152763.

28. Xia, S., Y. Yang, Q. Jia, M. Shang, L. Li, S. Chen, and W. Zhang, *Unlocking fast kinetics of n–p-type heterostructured MoS_2@PANI photocathode toward robust low-overpotential Li–O_2 batteries.* Inorganic Chemistry Frontiers, 2024. **11**(12): p. 3538-3547.

29. Chen, X., A. Zhang, H. Zou, L. Li, Q. Zhu, and W. Zhang, *Defect engineering modulated $MoSe_2$ cathode achieves highly effective photo-responsive zinc ion battery.* Energy Storage Materials, 2024. **70**: p. 103457.

30. Wang, R., K. He, J. Liu, Z. Liu, X. Lv, J. Su, and Y. Wen, *Enhanced structure stability and electrochemical performance of $LiNiO_2$ by Li_2SeO_4 coating and gradient surface SeO_3^{2-}/ SeO_4^{2-} doping.* Surface and Coatings Technology, 2023. **465**: p. 129587.

31. Wei, L., R. Sheng, Z. Liu, K. Cai, J. Su, X. Lv, and Y. Wen, *One-step synthesis of Li_2MoO_4-coated and Mo-doped $LiNi_{0.8}Co_{0.1}Mn_{0.1}O_2$ single-crystals using Li_2MoO_4 as a sacrificial molten salt.* Journal of Power Sources, 2023. **587**: p. 233703.

32. Yue, J., S. Chen, Y. Wang, A. Zhang, S. Li, X. Han, Z. Hu, R. Zhao, C. Wu, and Y. Bai, *Na^+ Preintercalated MoO_3 Microrods for Aqueous Zinc/Sodium Batteries with Enhanced Performance.* ACS Applied Materials & Interfaces, 2023. **15**(47): p. 54488-54498.

33. Xiao, X., C. Zhang, S. Lin, L. Huang, Z. Hu, Y. Cheng, T. Li, W. Qiao, D. Long, Y. Huang, L. Mai, Y. Gogotsi, and J. Zhou, *Intercalation of cations into partially reduced molybdenum oxide for high-rate pseudocapacitors.* Energy Storage Materials, 2015. **1**: p. 1-8.

34. Hu, Z., X. Zhang, C. Peng, G. Lei, and Z. Li, *Pre-intercalation of potassium to improve the electrochemical performance of carbon-coated* MoO_3 *cathode materials for lithium batteries.* Journal of Alloys and Compounds, 2020. **826**: p. 154055.

35. Yang, W., J. Xiao, Y. Ma, S. Cui, P. Zhang, P. Zhai, L. Meng, X. Wang, Y. Wei, and Z. Du, *Tin intercalated ultrathin* MoO_3 *nanoribbons for advanced lithium–sulfur batteries.* Advanced Energy Materials, 2019. **9**(7): p. 1803137.

36. Alimohammadi, F., D. Omo-Lamai, R. Andris, T. Averianov, Z. Wang, L. Wang, K. Kisslinger, E.S. Takeuchi, A.C. Marschilok, K.J. Takeuchi, and E. Pomerantseva, *Improving charge transport in integrated* MoO_3/C *electrode materials for water-in-salt energy storage systems by incorporating oxygen vacancies.* Journal of Power Sources, 2023. **583**: p. 233531.

37. Norouzi, N., D. Omo-Lamai, F. Alimohammadi, T. Averianov, J. Kuang, S. Yan, L. Wang, E. Stavitski, D. Leshchev, and K.J. Takeuchi, *The dopamine assisted synthesis of* MoO_3*/carbon electrodes with enhanced capacitance in aqueous electrolyte.* Frontiers in Chemistry, 2022. **10**: p. 873462.

38. Saraf, M., C.E. Shuck, N. Norouzi, K. Matthews, A. Inman, T. Zhang, E. Pomerantseva, and Y. Gogotsi, *Free-Standing* α*-*MoO_3/Ti_3C_2 *MXene Hybrid Electrode in Water-in-Salt Electrolytes.* Energy & Environmental Materials, 2023: p. e12516.

39. Yao, B., L. Huang, J. Zhang, X. Gao, J. Wu, Y. Cheng, X. Xiao, B. Wang, Y. Li, and J. Zhou, *Flexible transparent molybdenum trioxide nanopaper for energy storage.* Advanced Materials, 2016. **28**(30): p. 6353-6358.

40. Zakharova, G., C. Täschner, V. Volkov, I. Hellmann, R. Klingeler, A. Leonhardt, and B. Büchner, $MoO_{3-\delta}$ *nanorods: synthesis, characterization and magnetic properties.* Solid State Sciences, 2007. **9**(11): p. 1028-1032.

41. Floquet, N., O. Bertrand, and J. Heizmann, *Structural and morphological studies of the growth of* MoO_3 *scales during high-temperature oxidation of molybdenum.* Oxidation of metals, 1992. **37**: p. 253-280.

42. Li, W., F. Cheng, Z. Tao, and J. Chen, *Vapor-transportation preparation and reversible lithium intercalation/deintercalation of* α*-*MoO_3 *microrods.* The Journal of Physical Chemistry B, 2006. **110**(1): p. 119-124.

43. Yu, M., H. Shao, G. Wang, F. Yang, C. Liang, P. Rozier, C.-Z. Wang, X. Lu, P. Simon, and X. Feng, *Interlayer gap widened* α*-phase molybdenum trioxide as high-rate anodes for dual-ion-intercalation energy storage devices.* Nature Communications, 2020. **11**(1): p. 1348.

44. Zhang, H., W. Wu, Q. Liu, F. Yang, X. Shi, X. Liu, M. Yu, and X. Lu, *Interlayer Engineering of α-*MoO_3 *Modulates Selective Hydronium Intercalation in Neutral Aqueous Electrolyte.* Angewandte Chemie International Edition, 2021. **60**(2): p. 896-903.

45. Zhou, L., L. Yang, P. Yuan, J. Zou, Y. Wu, and C. Yu, *α-*MoO_3 *nanobelts: a high performance cathode material for lithium ion batteries.* The Journal of Physical Chemistry C, 2010. **114**(49): p. 21868-21872.

46. Hashem, A.M., H. Groult, A. Mauger, K. Zaghib, and C.M. Julien, *Electrochemical properties of nanofibers α-*MoO_3 *as cathode materials for Li batteries.* Journal of Power Sources, 2012. **219**: p. 126-132.

47. Kim, H.-S., J.B. Cook, H. Lin, Jesse S. Ko, Sarah H. Tolbert, V. Ozolins, and B. Dunn, *Oxygen vacancies enhance pseudocapacitive charge storage properties of* MoO_{3-x}. Nature Materials, 2017. **16**(4): p. 454-460.

48. Noerochim, L., J.-Z. Wang, D. Wexler, Z. Chao, and H.-K. Liu, *Rapid synthesis of free-standing* MoO_3*/Graphene films by the microwave hydrothermal method as cathode for bendable lithium batteries.* Journal of Power Sources, 2013. **228**: p. 198-205.

49. Zhang, H., X. Liu, R. Wang, R. Mi, S. Li, Y. Cui, Y. Deng, J. Mei, and H. Liu, *Coating of α-*MoO_3 *on nitrogen-doped carbon nanotubes by electrodeposition as a high-performance cathode material for lithium-ion batteries.* Journal of Power Sources, 2015. **274**: p. 1063-1069.